Supporting Information

High–entropy cathode catalyst with multiphase catalytic capability of Li$_2$O$_2$ and Li$_2$CO$_3$ enabling ultralong cycle life in Li–air batteries

Xia Li,[a] Guoliang Zhang,[a] Dongmei Zhang,[a] Ruonan Yang,[a] Han Yu,[a] Xiuqi Zhang,[a] Gang Lian,[b] Hua Hou,[c] Zhanhu Guo,[d] Chuanxin Hou,[e] Xiaoyang Yang,[e] and Feng Dang*[a]

[a]Key Laboratory for Liquid-Solid Structure Evolution and Processing of Materials (Ministry of Education), School of Materials Science and Engineering, Shandong University, Jinan 250061, China

[b]State Key Laboratory of Crystal Materials, Shandong University, Jinan 250061, P. R. China

[c]Shanxi-Zheda Institute of Advanced Materials and Chemical Engineering, Taiyuan 030024, P. R. China
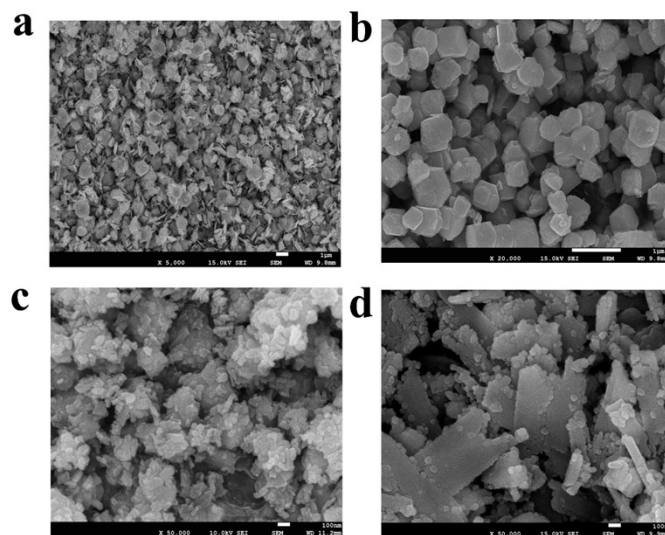
[d]Integrated Composites Lab, Department of Mechanical and Construction Engineering, Northumbria University, Newcastle Upon Tyne NE1 8ST, UK

[e]School of Environmental and Material Engineering, Yantai University, No.30 Qingquan Road, Yantai 264005, P. R. China

*Corresponding author: dangfeng@sdu.edu.cn
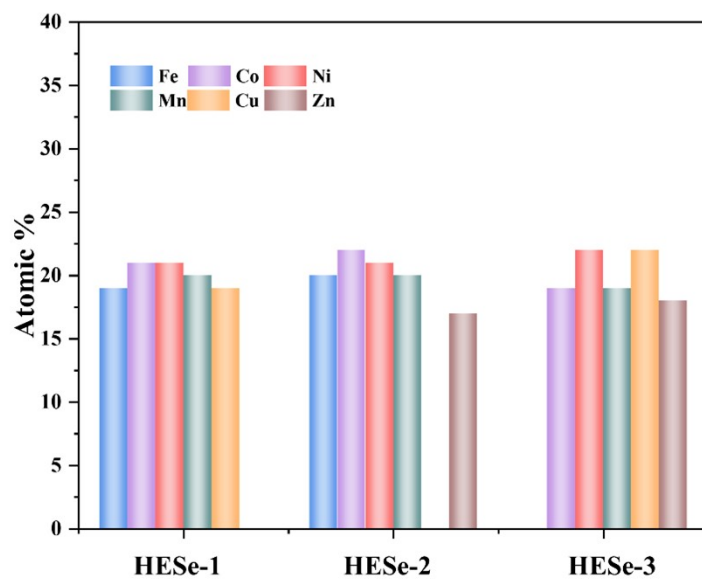
Figure S1. ICP-OES results for HESes

Figure S2. SEM images of a) (FeCoNi)Se$_2$, b) (FeCoNiMn)Se$_2$, c) HESe-1 and d) HESe-3
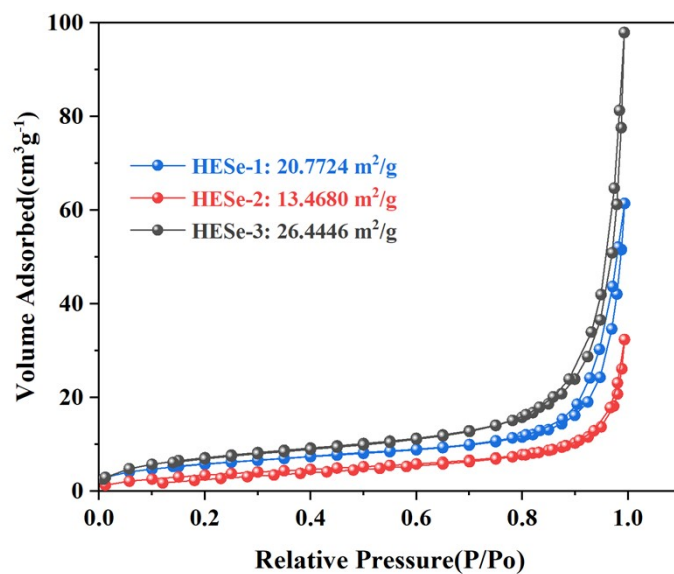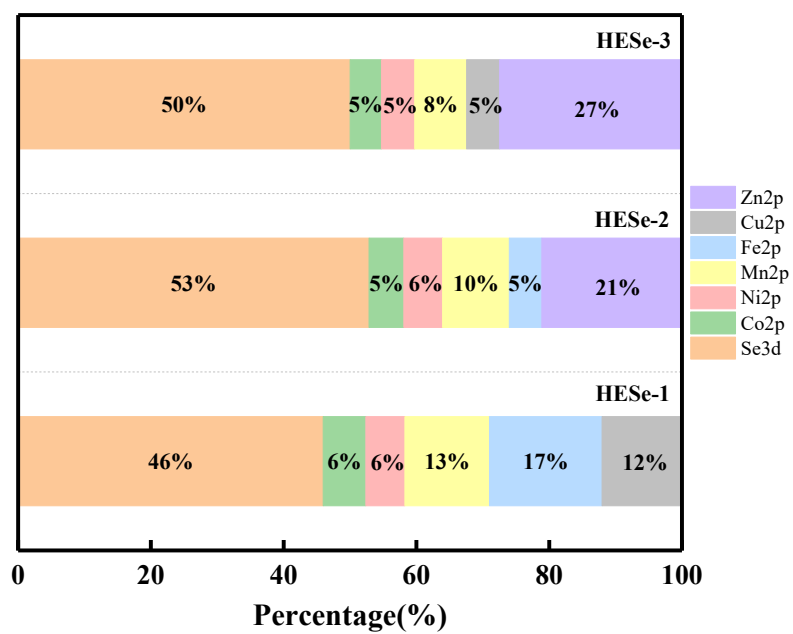
Figure S3. N_2 adsorption-desorption isotherms and pore size distribution profiles of HESe-1, HESe-2 and HESe-3.

Figure S4. XPS survey spectra of the HESe samples with calculated metal atomic ratio
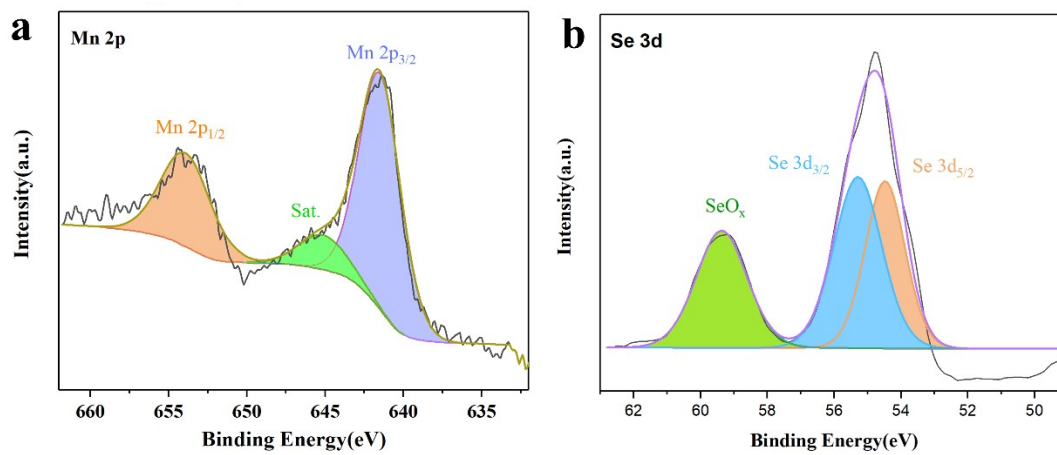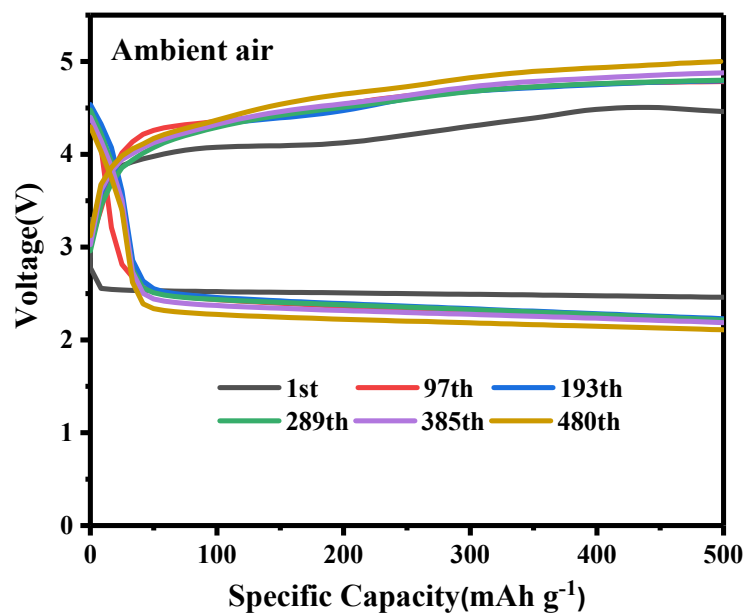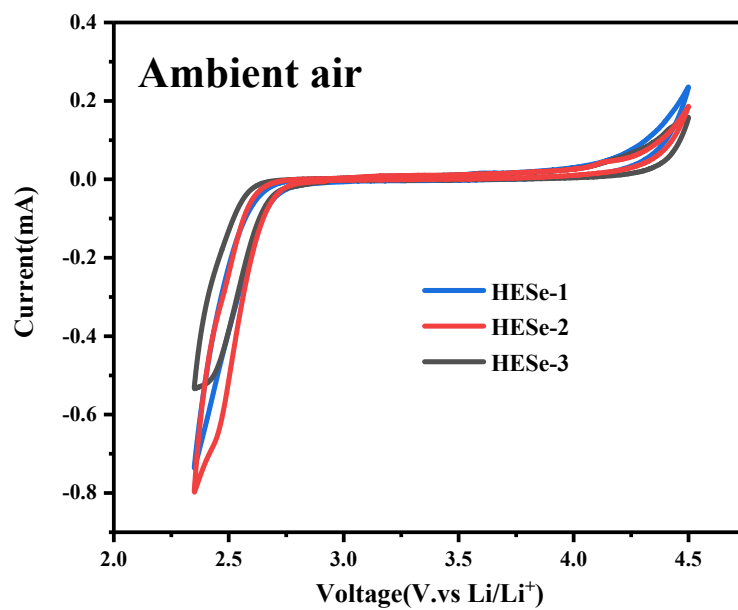
Figure S5. The XPS spectra of a) Mn b) Se in HESe-2.
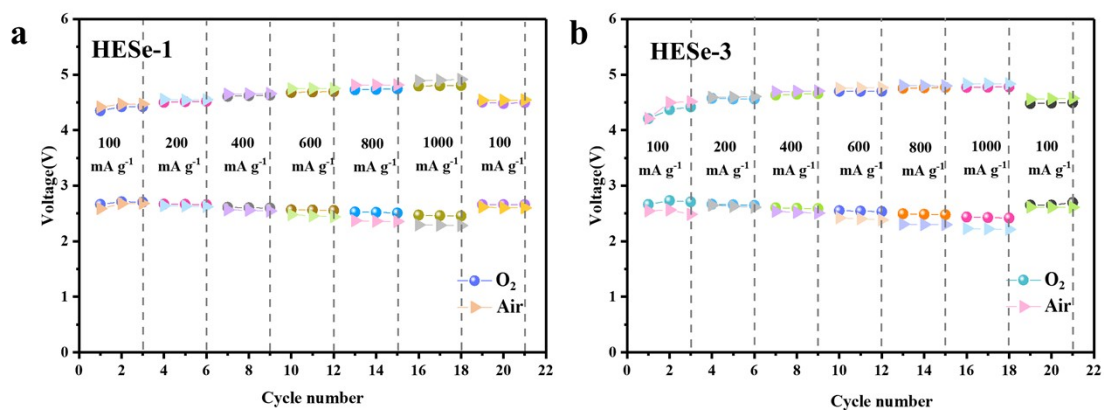
Figure S6. Cycling performances of HESe-2 cathode with selected typical discharge/charge profiles under a limited capacity of 500 mA h g^{-1} at 500 mA g^{-1} in LABs.

Figure S7. CV curves of the HESe cathodes under a scan rate of 0.1 mV s^{-1} with a voltage window of 2.35 ~ 4.5 V in ambient air

Figure S8. Rate performance of a) HESe-1 cathode and b) HESe-3 cathode at different current densities (100 to 1000 mA g^{-1}) with a limited specific capacity 500 mAh g^{-1} in O$_2$ and air.
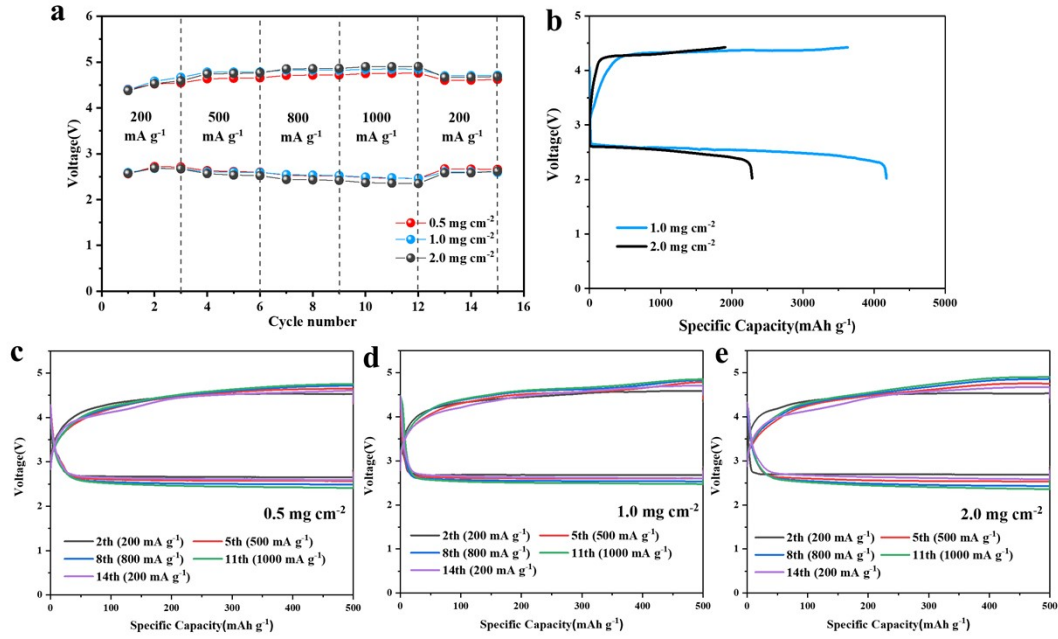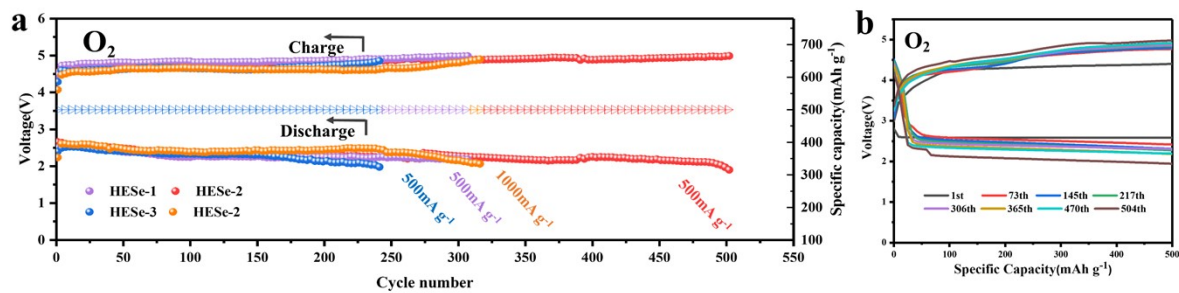
Figure S9. a) Rate performance of HESe-2 cathodes with different mass loadings at current densities (200 to 1000 mA g^{-1}) with a limited specific capacity 500 mAh g^{-1}; b) The initial discharge/charge profiles of HESe-2 cathodes with different mass loadings at 100 mA g^{-1} with a voltage range from 2 to 4.5 V; c) Rate performance of HESe-2 cathodes with selected typical discharge/charge profiles under mass loadings of c) 0.5 mg cm^{-2}, d) 1.0 mg cm^{-2} and e) 2.0 mg cm^{-2}.

As shown in Figure S9a and S9c-e, the HESe-2 cathode with the mass loading of 1.0 mg cm^{-2} exhibited almost the same discharge potentials and higher charge potentials at the currents 200-1000 mA g^{-1} and 500 mA h g^{-1} when compared to those of the cathode with 0.5 mg cm^{-2}. Meanwhile, the cathode with 2.0 mg cm^{-2} exhibited higher discharge/charge overpotentials at the same test conditions. With a cutoff voltage window of 2-4.5 V at 100 mA g^{-1}, HESe-2 cathode with 1.0 mg cm^{-2} delivered larger discharge capacity of 4173.3 mA h g^{-1} with a coulombic efficiency of 86.97% compared to the cathode with 0.5 mg cm^{-2} (Figure 3c). For the cathode with 2.0 mg cm^{-2}, the discharge capacity decreased to 2284.9 mA h g^{-1} with the coulombic efficiency of 83.46% (Figure S9b).

Figure S10. a) Cycling performances of HESe cathodes with terminal voltages at different current densities and fixed capacity 500 mAh g^{-1} in LOBs; b) Cycling performances of HESe-2 cathode with selected typical discharge/charge profiles under a limited capacity of 500 mA h g^{-1} at 500 mA g^{-1} in LOBs.
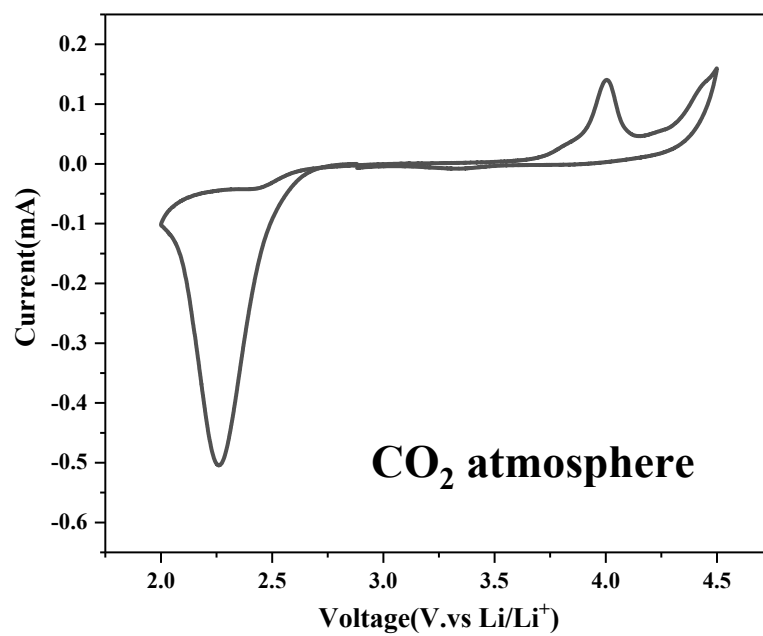
Figure S11. CV curve of the HESe cathode under a scan rate of 0.1 mV s^{-1} with a voltage window of 2.0 ~ 4.5 V in CO_2 atmosphere
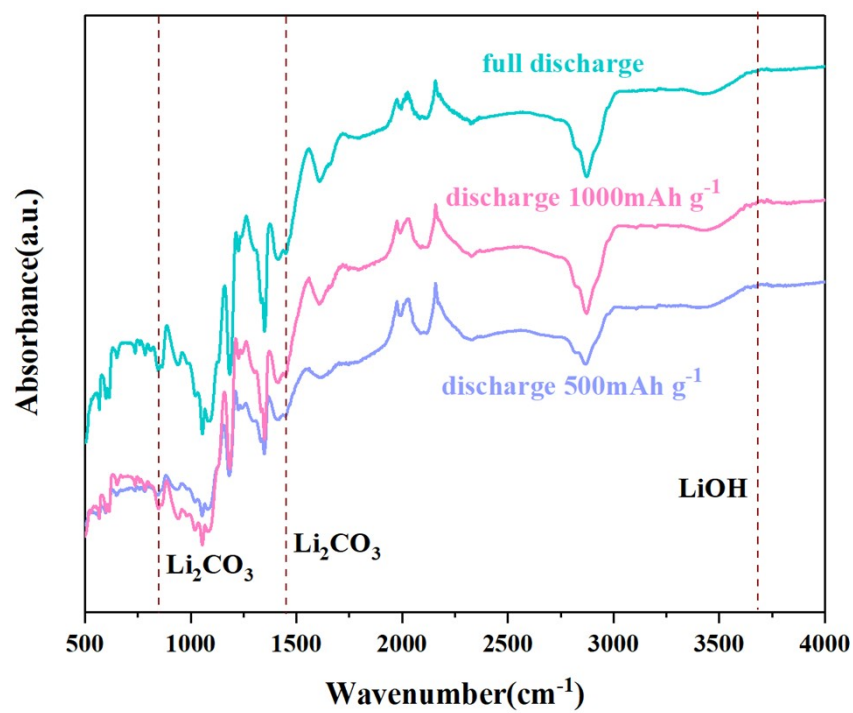
Figure S12. FTIR spectra of discharging to different capacities in ambient air
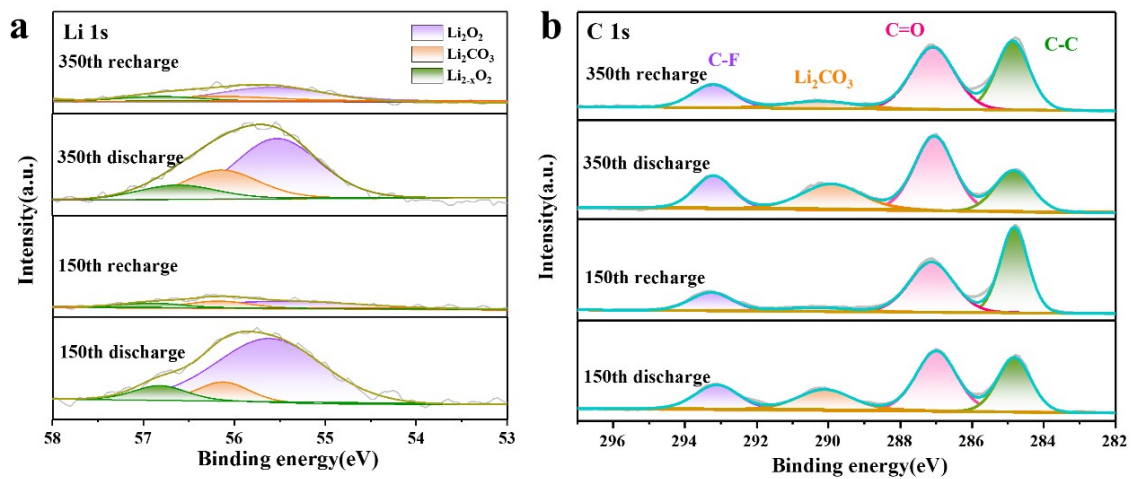
Figure S13. XPS spectra of a) Li 1s and b) C 1s of HESe electrode at different discharge/charge stages in ambient air.
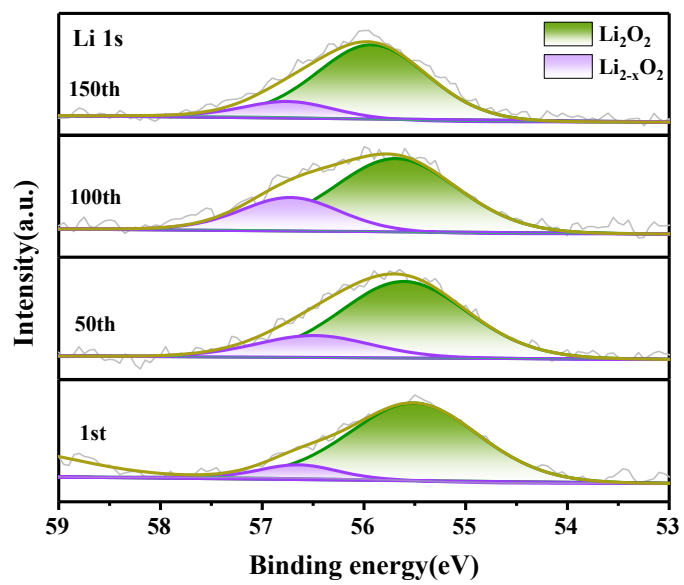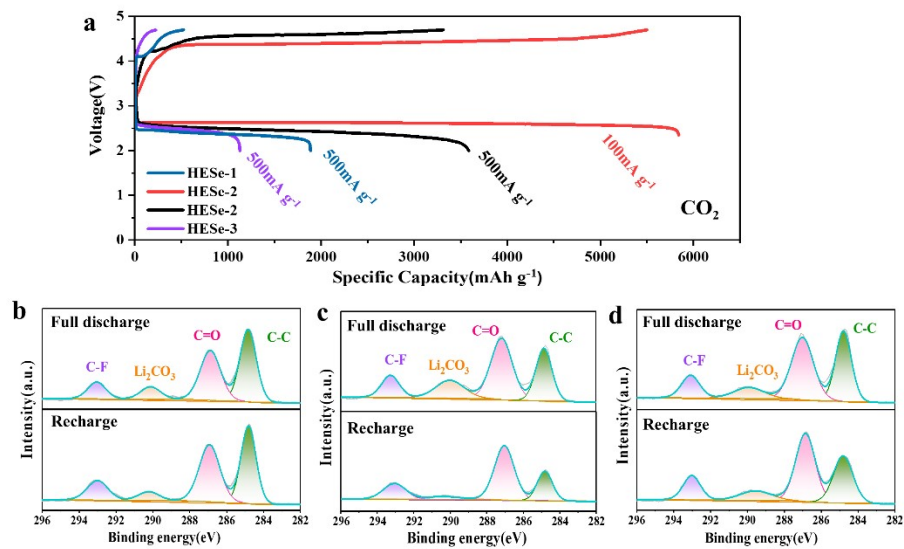
Figure S14. XPS spectra of Li 1s in O_2

Figure S15. a) The discharge/charge profiles of HESe cathodes in LCBs; XPS spectra of C 1s in b) HESe-1, c) HESe-2 and d) HESe-3 in LCBs after full discharge and recharge at 500 mA g^{-1}.
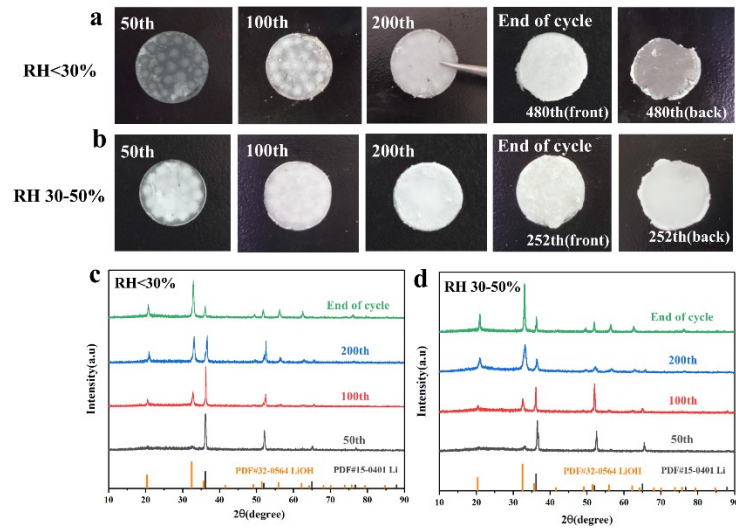
Figure S16. Li anode pictures at different cycles of a) low humidity (RH<30%) and b) high humidity (RH 30-50%); c) XRD patterns of Li anode during cycling under c) low humidity and d) high humidity.
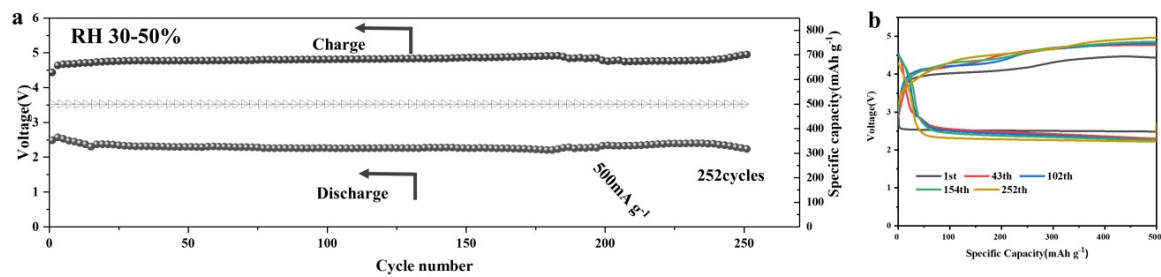
Figure S17. a) Cycling performance of HESe cathode with terminal voltages at 500 mA g^{-1} and fixed capacity 500 mAh g^{-1} in LABs at high humidity (RH 30-50%); b) Cycling performance of HESe cathode with selected typical discharge/charge profiles under a limited capacity of 500 mA h g^{-1} at 500 mA g^{-1}.
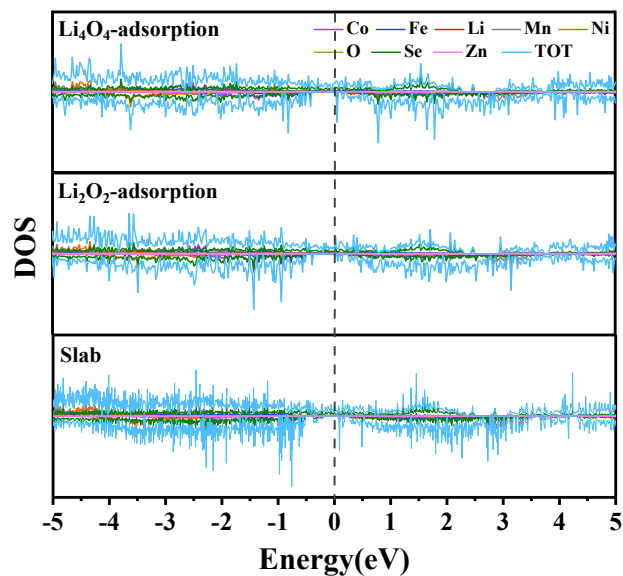
Figure S18. Density of states (DOS) of pristine, after adsorption of Li_2O_2 groups and after adsorption of Li_4O_4 groups.

The electronic states of the (210) facet at the Fermi level increased after the adsorption of discharge products (Li_2O_2 and Li_4O_4), indicating the improved conductivity of the adsorbed system, in which the O 2p, Se 3d, and TM 3d orbitals contributed to the electronic states near the Fermi level to the growth of Li_2O_2, improving charge transfer efficiency and resulting in good catalytic durability.
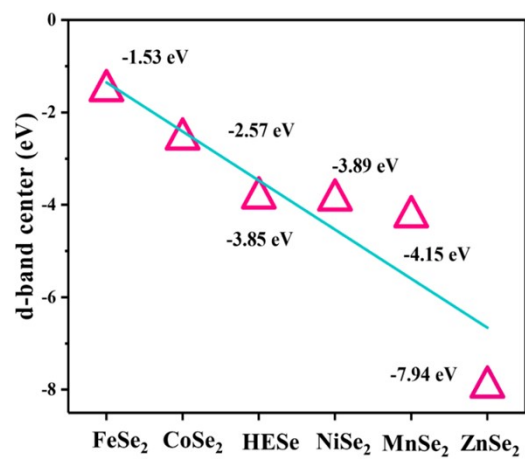
Figure S19. The d-band centers of $FeSe_2$, $CoSe_2$, HESe, $NiSe_2$, $MnSe_2$ and $ZnSe_2$.
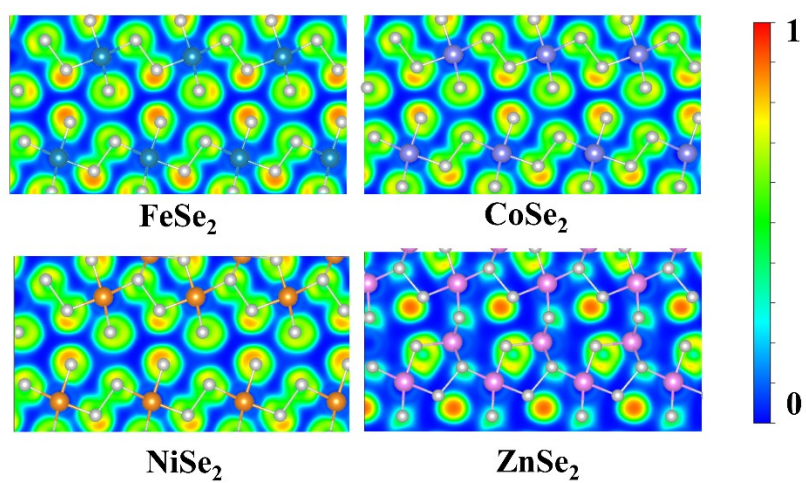
Figure S20. Electron localization function plots of FeSe$_2$, CoSe$_2$, NiSe$_2$ and ZnSe$_2$, respectively
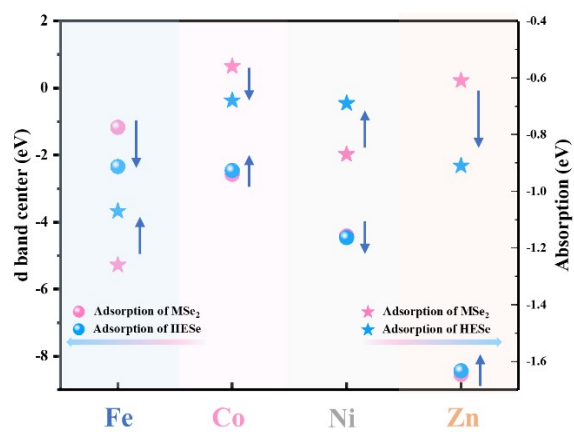
Figure S21. The relationship between d-band center and adsorption energy of different metal sites in MSe$_2$ and HESe
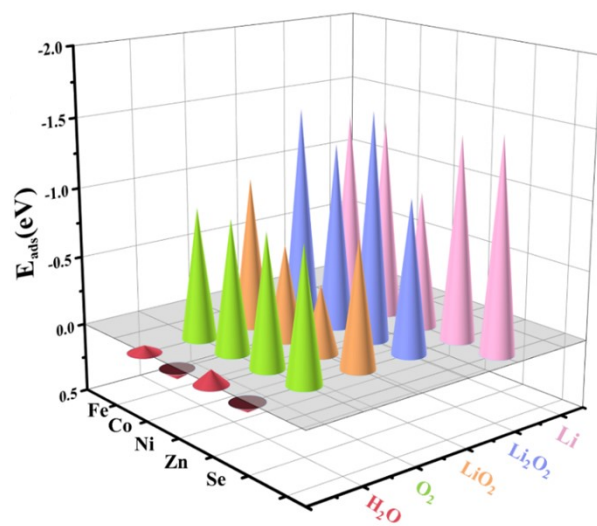
Figure S22. Adsorption energy of different reaction species on Fe, Co, Ni, Zn and Se sites.
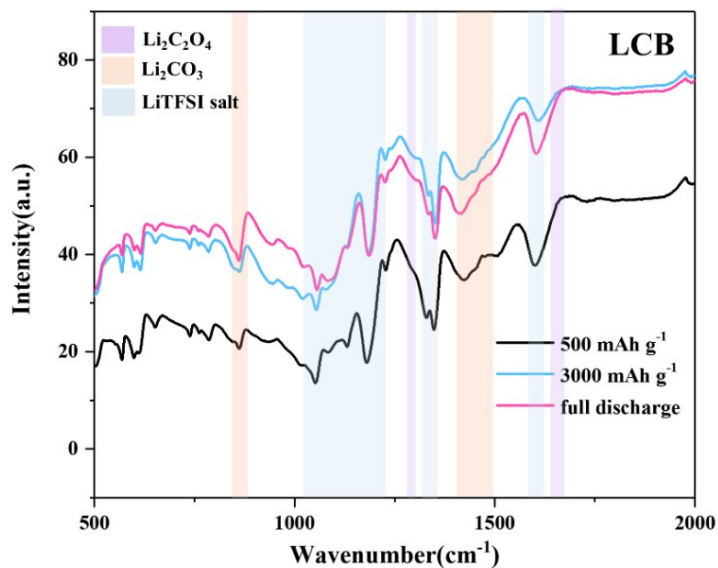
Figure S23. FTIR spectra of the HESe electrode at different capacities during discharge in LCB.

Figure S17 shows the FT-IR spectra tested in CO_2. No intermediate $Li_2C_2O_4$ is observed in the discharge products of Li-CO_2 batteries (1318, 1642 cm^{-1}).[1] The LiTFSI/TEGDME electrolyte typical peaks were found at 1040 to 1350 cm^{-1}.[2] Besides, the peaks at 1441, 1500 cm^{-1} can be attributed to Li_2CO_3.[3]
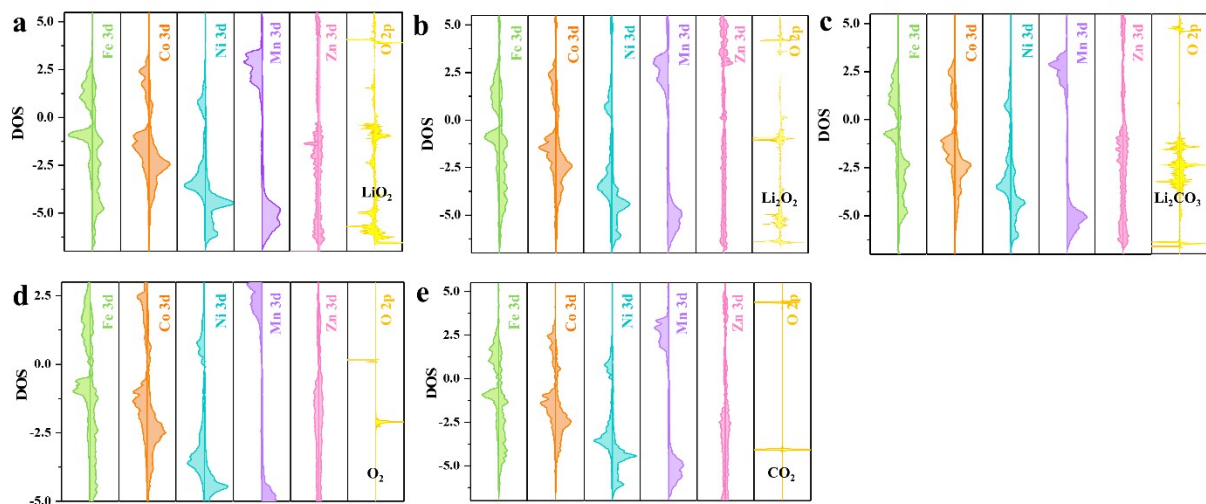
Figure S24. PDOS of metal's 3d orbitals and O 2p orbitals after adsorbed a) LiO_2, b) Li_2O_2, c) Li_2CO_3, d) O_2 and e) CO_2

config1　　config2　　config3　　config4　　config5　　config6　　config7

config8　　config9　　config10　　config11　　config12　　config13　　config14

config15　　config16　　config17　　config18　　config19　　config20　　config21

config22　　config23　　config24　　config25　　config26　　config27　　config28

Figure S25. Calculated different configurations
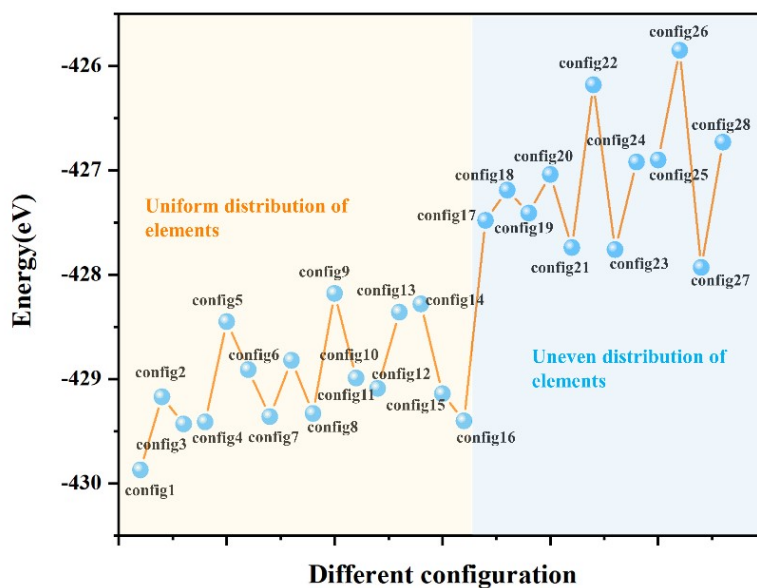
Figure S26. Calculated 28 configurations and corresponding surface energies
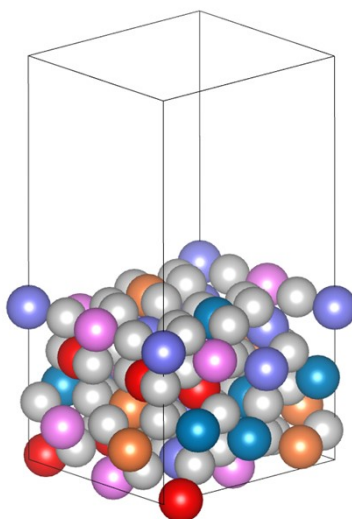
Figure S27. The structure model of config1

We constructed the HESe (210) plane model with a metal atom ratio of 1:1:1:1:1 for /Fe/Co/Ni/Mn/Zn. Due to the large number of possible configurations and limited computational resources, 28 representative configurations were selected for optimization. Elements in configurations 1-16 are relatively evenly distributed, resulting in lower calculated energies. Among them, configuration 1 has the lowest energy and is characterized by a slight surface excess of Co and no surface-exposed Mn. It can also be observed that the clustering of Co atoms seems to be beneficial for energy reduction and Mn plays an important role in stabilizing the HESe structure. Configurations 18-28 exhibit segregation of multiple elements, making the structures unstable and resulting in higher energies.

Table S1. Comparison of the electrochemical performance of different electrodes using in Lithium-air battery[4-20]

Materials	Assistance Strategy				circumstance	Mass(mg/cm^{-2})	Specific Capacity (mAh g^{-1})	Cycle Performance		Ref
	Electrolyte	Ionic liquid or Redox mediators additive	Li Anode	Oxygen-selective membranes				Current density (mA g^{-1}) /Limited Capacity (mAh g^{-1})	Cycle Number	
CNT-SS	Zeolite X	LiTFSI in [C$_2$C$_1$im][NTf$_2$]			Ambient air	0.05	12,020（500 mA g^{-1}）	500/500	309 162(with ionic liquid electrolytes)	4
MCNTs@MnO$_2$	Commercial electrolyte	Co^{II}-salen			dry air (21% O$_2$, 78% N$_2$) without CO$_2$ and H$_2$O	0.3-0.5	13050(500 mA g^{-1})	500/1000	300 60(only with catalyst)	5
MoS$_2$	LiTFSI/ DMSO	EMIM-BF4	Li$_2$CO$_3$/C-coated		79%N$_2$, 21%O$_2$, 500ppm. CO$_2$ RH=45%	0.1		500/500	550 11（without anode-protection layer）	6
CNT	Commercial electrolyte	DBBQ and TEMPO		PSS-Li/GO-Li/GF	Ambient air RH=25%	0.45 ± 0.1		0.2 mA cm^{-2}/ 0.2mAh cm^{-2}	486 100（single-cathode）	7
rGO	LiTFSI TEGDME gel polymer electrolyte containing LiI and 4 wt% SiO$_2$	LiI	rGO protected Li anode	SiO$_2$–LiI-GPE	Ambient air RH=15%	0.8–1.0		100/500	100 50(without LiI）	8
MnO	gel electrolyte		LiEDA protected Li anode		Ambient air RH=10-40%	0.4-0.5		200/500	235 134（with liquid electrolyte）	9
Mo$_3$P/ TEMPO	LiTFSI/ DMSO	EMIM-BF4/ TEMPO DBBQ	Li$_2$CO$_3$/C-coated		78%N$_2$, 21%O$_2$, 500 ppm. CO$_2$, RH=45%	0.1		500/500	1200 150 (without protection)	10
3DOS-Co@Mn@CC	Gel Electrolyte				Ambient air RH=50%	0.63	6500(500 mA g^{-1})	500/500	100	11

Material	Electrolyte				Atmosphere	Mass loading	Capacity	Current density	Cycles	Ref.
Gr-Co$_3$O$_4$	LiPF6 in ethylene carbonate (EC) and diethyl carbonate (DEC)				Ambient air	0.325		160/200	50	12
SWNT/IL CNG	Li[NTf$_2$] and [C$_2$C$_1$im][NTf$_2$] solution				Ambient air	0.6	10730（200）	200/1000	10	13
NiCo$_2$O$_4$@Ni	LiPF6/EC/DEC				Ambient air	1.0		0.5 mA cm^{-2}/ 1 mAh cm^{-2}	100	14
Fe$_2$Mo$_3$O$_2$	Commercial electrolyte				Ambient air	1.0	8000（500 mA g^{-1}）	500/600	157	15
CoMoO$_4$	Commercial electrolyte				Ambient air RH<30%	1.0	12000（100 mA g^{-1}）	500/600 1000/600	247 270	16
RuO$_2$/NiO	Commercial electrolyte				Ambient air RH=65%	0.075	3465 （250 mA g^{-1}）	250/500	200	17
SnO$_2$@C	Commercial electrolyte				Ambient air	0.158	8339 （75 mA g^{-1}）	75/1000 200/1000	31 25	18
Fe@La$_{0.6}$Sr$_{0.4}$Co$_{0.2}$Fe$_{0.8}$O$_3$	LiTFSI/DMSO				Ambient air	1.0	14093(200 mA g^{-1})	400/500	156	19
NiCo$_2$O$_4$	Commercial electrolyte				Ambient air (25℃ CO$_2$ 0.03%)	0.8	8019	300/1000	40	20
HESe	**Commercial electrolyte**	**No**	**No**	**No**	**Ambient air**	**0.5**	**3650（100 mA g^{-1}）**	**500/500**	**480**	**This work**

Table S2. Comparison of the electrochemical performance of different electrodes using in Lithium-CO$_2$ battery[21-39]

Materials	Electrolyte	Mass(mg/cm^{-2})	Specific Capacity (mAh g^{-1})	Current density (mA g^{-1}) /Limited Capacity (mAh g^{-1})	Cycle Number	ref
RuP$_2$-NPCF	LiTFSI/TEGDME	0.15–0.25	11951(100 mA g^{-1})	200/1000	200	21
RuCo/CNFs	LiTFSI in DMSO	0.25	17 270(300 mA g^{-1})	500/1000	90	22
IrO$_2$-N/CNT	LiTFSI in TEGDME	0.2–0.3	4634(100 mA g^{-1})	100/400	316	23
NiS$_2$/FeS$_2$-NSGA	LiTFSI in DMSO	0.25	21,178(300 mA g^{-1})	1000/1000	127	24
ZnCo$_2$O$_4$@CNTs	LiTFSI in TEGDME	0.2	4275(100 mA g^{-1})	100/500	200	25
Co–N-CNTs	LiTFSI in TEGDME		6042(200 mA g^{-1})	400/500	92	26
Ir NSs-CNFs	LiTFSI in TEGDME	0.3	7666.7(166.7 mA g^{-1})	500/1000	400	27
MnO@NC-G	LiTFSI in TEGDME	0.27-0.45	25021(50 mA g^{-1})	1000/1000	200	28
ZnS QDs/N-rGO	LiTFSI in TEGDME	0.2-0.5	10310(100 mA g^{-1})	400/1000	400	29
Co-Doped MnO$_2$	LiTFSI in TEGDME	0.5-0.8	8203(100 mA g^{-1})	100/1000	500	30
O$_V$-TiO$_2$/MXene	LiTFSI in TEGDME		18042.5(200 mA g^{-1})	200/1000	158	31
N-CNTs@Ti	LiTFSI in TEGDME	0.45	9292.3(50 mA g^{-1})	250/1000	45	32
MoS$_2$ NFs	0.1 M LiTFSI in (EMIM-BF4)/DMSO (25%/75%)	0.1 ±0.002	60000(100 mA g^{-1})	500/500	500	33
MoS$_2$/CNT	LiTFSI in TEGDME		8551(100 mA g^{-1})	100/500	142	34
Fe-ISA/N,S-HG	1 M LiTFSI 0.3 M LiNO$_3$/DMSO	0.21	23174(100 mA g^{-1})	1000/1000	210	35
Cu–NG	LiTFSI/TEGDME	0.27-0.44	13 676(200 mA g^{-1})	200/1000	50	36
BN-hG	LiTFSI in TEGDME	0.3	16033(300 mA g^{-1})	1000/1000	200	37
B-NCNT	LiTFSI in TEGDME	0.2	23 328(50 mA g^{-1})	1000/1000	360	38
Ir-Te NWs	LiNO3-DMSO	0.4-0.6	13,247.1(200 mA g^{-1})	1000/500	350	39
HESe	**LiTFSI in TEGDME**	**0.5**		**500/500**	**1050**	**This work**
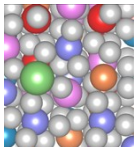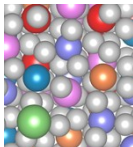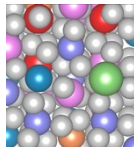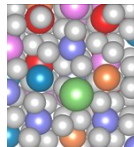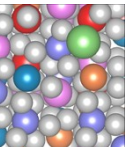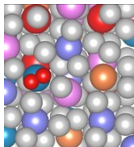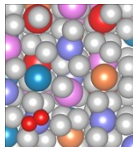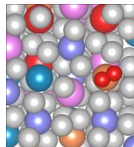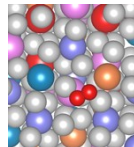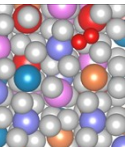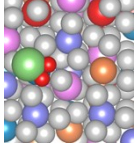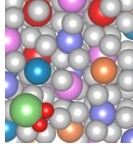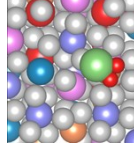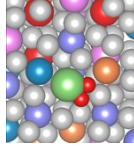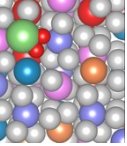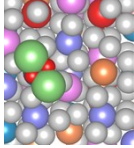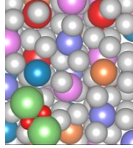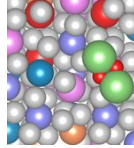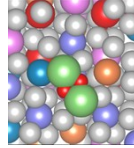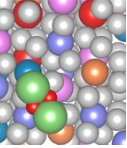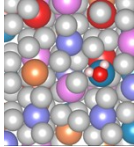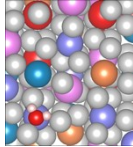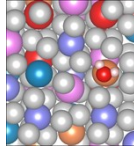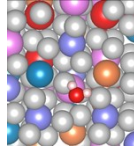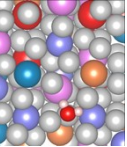
Table S3. d-band center (eV) of each metal site in MSe$_2$ and HESe

	Fe	Co	Ni	Mn	Zn
MSe$_2$	-1.17	-2.57	-4.41	-3.98	-8.54
HESe	-2.34	-2.46	-4.46	-4.84	-8.43

Table S4. LiO$_2$ adsorption energy (eV) on metal sites in MSe$_2$ and HESe

	Fe	Co	Ni	Mn	Zn
MSe$_2$	-1.26	-0.56	-0.87	-1.26	-0.61
HESe	-1.07	-0.68	-0.69	-1.07	-0.91

Table S5. Structure models and corresponding adsorption energies of different adsorbed species on different adsorption sites of HESe (210) facet

Adsorption Sites	Fe	Co	Ni	Zn	Se
sub- Li* （eV）	 -1.401	 -1.419	 -0.977	 -1.4567	 -1.526
sub- O$_2$* （eV）	 -0.940	 -0.944	 -0.943	 -0.956	 -0.942
sub- LiO$_2$* （eV）	 -1.070	 -0.683	 -0.490	 -0.907	 -0.665
sub- Li$_2$O$_2$* （eV）	 -1.510	 -1.322	 -1.618	 -1.092	 -1.551
Sub- H$_2$O* （eV）	 -0.054	 0.076	 -0.107	 0.069	 0.055

References:

1. W. Zhong, C. Zhang, S. Li, W. Zhang, Z. Zeng, S. Cheng and J. Xie, *Science China Materials*, 2022, **66**, 903-912.
2. S. Ramesh and C.-W. Liew, *Measurement*, 2013, **46**, 1650-1656.
3. J. J. Xu, Z. W. Chang, Y. Wang, D. P. Liu, Y. Zhang and X. B. Zhang, *Advanced Materials*, 2016, **28**, 9620-9628.
4. X. Chi, M. Li, J. Di, P. Bai, L. Song, X. Wang, F. Li, S. Liang, J. Xu and J. Yu, *Nature*, 2021, **592**, 551-557.
5. X. Hu, J. Wang, Z. Li, J. Wang, D. H. Gregory and J. Chen, *Nano Letters*, 2017, **17**, 2073-2078.
6. M. Asadi, B. Sayahpour, P. Abbasi, A. T. Ngo, K. Karis, J. R. Jokisaari, C. Liu, B. Narayanan, M. Gerard, P. Yasaei, X. Hu, A. Mukherjee, K. C. Lau, R. S. Assary, F. Khalili-Araghi, R. F. Klie, L. A. Curtiss and A. Salehi-Khojin, *Nature*, 2018, **555**, 502-506.
7. Q. Han, W. Guo, X. He, T. Liu, X. Liu, X. Zhu, T. Bian, L. Jiang, J. Lu and Y. Zhao, *Joule*, 2022, **6**, 381-398.
8. Z. Guo, J. Li, Y. Xia, C. Chen, F. Wang, A. G. Tamirat, Y. Wang, Y. Xia, L. Wang and S. Feng, *Journal of Materials Chemistry A*, 2018, **6**, 6022-6032.
9. X. Lei, X. Liu, W. Ma, Z. Cao, Y. Wang and Y. Ding, *Angewandte Chemie International Edition*, 2018, **57**, 16131-16135.
10. A. Kondori, Z. Jiang, M. Esmaeilirad, M. Tamadoni Saray, A. Kakekhani, K. Kucuk, P. Navarro Munoz Delgado, S. Maghsoudipour, J. Hayes, C. S. Johnson, C. U. Segre, R. Shahbazian-Yassar, A. M. Rappe and M. Asadi, *Advanced Materials*, 2020, **32**.
11. J. Li, Z. Wang, L. Yang, Y. Liu, Y. Xing, S. Zhang and H. Xu, *ACS Applied Materials & Interfaces*, 2021, **13**, 18627-18637.
12. C. Sun, F. Li, C. Ma, Y. Wang, Y. Ren, W. Yang, Z. Ma, J. Li, Y. Chen, Y. Kim and L. Chen, *J. Mater. Chem. A*, 2014, **2**, 7188-7196.
13. T. Zhang and H. Zhou, *Angewandte Chemie International Edition*, 2012, **51**, 11062-11067.
14. L. Li, S.-H. Chai, S. Dai and A. Manthiram, *Energy & Environmental Science*, 2014, **7**.
15. Y. Qiu, G. Li, H. Zhou, G. Zhang, L. Guo, Z. Guo, R. Yang, Y. Fan, W. Wang, Y. Du and F. Dang, *Adv Sci (Weinh)*, 2023, **10**, e2300482.
16. H. Zhou, L. Guo, R. Zhang, L. Xie, Y. Qiu, G. Zhang, Z. Guo, B. Kong and F. Dang, *Advanced Functional Materials*, 2023, **33**.
17. P. Tan, Z. H. Wei, W. Shyy, T. S. Zhao and X. B. Zhu, *Energy & Environmental Science*, 2016, **9**, 1783-1793.
18. D. Mei, X. Yuan, Z. Ma, P. Wei, X. Yu, J. Yang and Z.-F. Ma, *ACS Applied Materials & Interfaces*, 2016, **8**, 12804-12811.
19. J. Cheng, Y. Jiang, M. Zhang, Y. Sun, L. Zou, B. Chi, J. Pu and L. Jian, *ChemCatChem*, 2018, **10**, 1635-1642.
20. L. Zou, Y. Jiang, J. Cheng, Y. Gong, B. Chi, J. Pu and L. Jian, *Electrochimica Acta*, 2016, **216**, 120-129.
21. Z. Guo, J. Li, H. Qi, X. Sun, H. Li, A. G. Tamirat, J. Liu, Y. Wang and L. Wang, *Small*, 2018, **15**.
22. Y. Jin, F. Chen and J. Wang, *ACS Sustainable Chemistry & Engineering*, 2020, **8**, 2783-2792.
23. G. Wu, X. Li, Z. Zhang, P. Dong, M. Xu, H. Peng, X. Zeng, Y. Zhang and S. Liao, *Journal of Materials Chemistry A*, 2020, **8**, 3763-3770.
24. Y. Jin, Y. Liu, L. Song, J. Yu, K. Li, M. Zhang and J. Wang, *Chemical Engineering Journal*, 2022, **430**.
25. S. Thoka, C.-J. Chen, A. Jena, F.-M. Wang, X.-C. Wang, H. Chang, S.-F. Hu and R.-S. Liu, *ACS applied materials & interfaces*, 2020, **12**, 17353-17363.

26. L. Song, T. Wang, C. Wu, X. Fan and J. He, *Chemical Communications*, 2019, **55**, 12781-12784.

27. Y. Xing, Y. Yang, D. Li, M. Luo, N. Chen, Y. Ye, J. Qian, L. Li, D. Yang, F. Wu, R. Chen and S. Guo, *Advanced Materials*, 2018, **30**.

28. S. Li, Y. Liu, J. Zhou, S. Hong, Y. Dong, J. Wang, X. Gao, P. Qi, Y. Han and B. Wang, *Energy & Environmental Science*, 2019, **12**, 1046-1054.

29. H. Wang, K. Xie, Y. You, Q. Hou, K. Zhang, N. Li, W. Yu, K. P. Loh, C. Shen and B. Wei, *Advanced Energy Materials*, 2019, **9**.

30. B. Ge, Y. Sun, J. Guo, X. Yan, C. Fernandez and Q. Peng, *Small*, 2019, **15**.

31. H. Wang, R. Zheng, C. Shu and J. Long, *ChemElectroChem*, 2020, **7**, 4922-4930.

32. Y. Li, J. Zhou, T. Zhang, T. Wang, X. Li, Y. Jia, J. Cheng, Q. Guan, E. Liu, H. Peng and B. Wang, *Advanced Functional Materials*, 2019, **29**.

33. A. Ahmadiparidari, R. E. Warburton, L. Majidi, M. Asadi, A. Chamaani, J. R. Jokisaari, S. Rastegar, Z. Hemmat, B. Sayahpour, R. S. Assary, B. Narayanan, P. Abbasi, P. C. Redfern, A. Ngo, M. Vörös, J. Greeley, R. Klie, L. A. Curtiss and A. Salehi-Khojin, *Advanced Materials*, 2019, **31**.

34. C.-J. Chen, C.-S. Huang, Y.-C. Huang, F.-M. Wang, X.-C. Wang, C.-C. Wu, W.-S. Chang, C.-L. Dong, L.-C. Yin and R.-S. Liu, *ACS Applied Materials & Interfaces*, 2021, **13**, 6156-6167.

35. C. Hu, L. Gong, Y. Xiao, Y. Yuan, N. M. Bedford, Z. Xia, L. Ma, T. Wu, Y. Lin, J. W. Connell, R. Shahbazian-Yassar, J. Lu, K. Amine and L. Dai, *Advanced Materials*, 2020, **32**.

36. Z. Zhang, Z. Zhang, P. Liu, Y. Xie, K. Cao and Z. Zhou, *Journal of Materials Chemistry A*, 2018, **6**, 3218-3223.

37. L. Qie, Y. Lin, J. W. Connell, J. Xu and L. Dai, *Angewandte Chemie International Edition*, 2017, **56**, 6970-6974.

38. X. Li, J. Zhou, J. Zhang, M. Li, X. Bi, T. Liu, T. He, J. Cheng, F. Zhang, Y. Li, X. Mu, J. Lu and B. Wang, *Advanced Materials*, 2019, **31**.

39. Y. Zhai, H. Tong, J. Deng, G. Li, Y. Hou, R. Zhang, J. Wang, Y. Lu, K. Liang, P. Chen, F. Dang and B. Kong, *Energy Storage Materials*, 2021, **43**, 391-401.